Pure Rotational CARS Thermometry Studies of Low Temperature Oxidation Kinetics in Air and Ethene-Air Nanosecond Pulse Discharge Plasmas

Yvette Zuzeek, Igor V. Adamovich, and Walter R. Lempert

Michael A. Chaszeyka Nonequilibrium Thermodynamics Laboratories,
Department of Mechanical Engineering,
The Ohio State University, Columbus, OH 43210

ABSTRACT

Pure rotational CARS thermometry is used to study low-temperature plasma assisted fuel oxidation kinetics in a repetitive nanosecond pulse discharge in ethene-air at stoichiometric and fuel lean conditions at 40 Torr pressure. Air and fuel-air mixtures are excited by a burst of high-voltage nanosecond pulses (peak voltage 20 kV, pulse duration ~25 nanosecond) at a 40 kHz pulse repetition rate and burst repetition rate of 10 Hz. The number of pulses in the burst is varied from a few pulses to a few hundred pulses. The results are compared to the previously developed hydrocarbon-air plasma chemistry model, modified to incorporate non-empirical scaling of the nanosecond discharge pulse energy coupled to the plasma with the number density, as well as one-dimensional conduction heat transfer. Experimental time-resolved temperature, determined as a function of number of pulses in the burst, is found to agree well with the model predictions. The results demonstrate that the heating rate in fuel-air plasmas is much faster compared to air plasmas, primarily due to energy release in exothermic reactions of fuel with O atoms generated by the plasma. It is found that the initial heating rate in fuel-air plasmas is controlled by the rate of radical (primarily O atoms) generation and is nearly independent of the equivalence ratio. At long burst durations, heating rate in lean fuel air-mixtures is significantly reduced when all fuel is oxidized.

Report Documentation Page

Form Approved
OMB No. 0704-0188

1. REPORT DATE	2. REPORT TYPE	3. DATES COVERED
2010		**00-00-2010 to 00-00-2010**

4. TITLE AND SUBTITLE	5a. CONTRACT NUMBER
Pure Rotational CARS Thermometry Studies of Low Temperature Oxidation Kinetics in Air and Ethene-Air Nanosecond Pulse Discharge Plasmas	5b. GRANT NUMBER
	5c. PROGRAM ELEMENT NUMBER
6. AUTHOR(S)	5d. PROJECT NUMBER
	5e. TASK NUMBER
	5f. WORK UNIT NUMBER
7. PERFORMING ORGANIZATION NAME(S) AND ADDRESS(ES) **Ohio State University,Columbus,OH,43210-1107**	8. PERFORMING ORGANIZATION REPORT NUMBER
9. SPONSORING/MONITORING AGENCY NAME(S) AND ADDRESS(ES)	10. SPONSOR/MONITOR'S ACRONYM(S)
	11. SPONSOR/MONITOR'S REPORT NUMBER(S)

12. DISTRIBUTION/AVAILABILITY STATEMENT
Approved for public release; distribution unlimited

13. SUPPLEMENTARY NOTES
accepted for publication in Journal of Physics D: Applied Physics

14. ABSTRACT
see report

15. SUBJECT TERMS

16. SECURITY CLASSIFICATION OF:			17. LIMITATION OF ABSTRACT	18. NUMBER OF PAGES	19a. NAME OF RESPONSIBLE PERSON
a. REPORT **unclassified**	b. ABSTRACT **unclassified**	c. THIS PAGE **unclassified**	**Same as Report (SAR)**	**39**	

1. Introduction

The last decade has seen greatly increased activity in the general discipline that has come to be known as plasma assisted combustion (PAC). Driven by a need to develop more efficient ignition and flame holding systems that can operate over a wide range of pressures, flow velocities, and equivalence ratios, numerous groups have reported the use of a variety of non-equilibrium discharge-based ignition techniques and devices, a thorough recent review of which has been recently presented by Starikovskaia [1]. One particular approach, which offers several advantages over conventional dc, rf, and microwave discharges, is to utilize high peak voltage nanosecond pulse duration discharges, operated at high pulse repetition rate, on the order of 10 – 100 kHz. Such discharges are characterized by inherently high reduced electric fields, E/n, up to several hundred Townsend (Td). At these high reduced fields strengths a significant fraction of the total discharge energy goes into molecular dissociation and population of excited electronic states. Repetitively pulsed nanosecond discharges exhibit increased stability at significantly higher pressures compared to other types of electric discharges, due to the inherent very low duty cycle operation. The basic idea is to operate the discharge with individual pulse duration that is much shorter than characteristic time scales for onset of ionization instabilities, and with pulse repetition rate that is greater than the rate of plasma decay. Such an approach enables the generation of large volume, diffuse discharges at relatively high pressures, on the order of a 100 Torr (13900 Pa) in nitrogen, air, and oxygen-helium mixtures [2,3].

Several groups have recently reported the use of nanosecond pulse discharges for fundamental studies of plasma enhanced combustion [4]. For example, Bozhenkov et al. [5] have shown significant ignition delay time reduction (by more than on order of magnitude) using a single pulse nanosecond discharge in H_2/air mixtures diluted in argon and preheated to ~900 K in a shock tube. Kim et al. [6] have reported large increases in the critical co-flow velocity, leading to lift-off of a methane-air jet diffusion flame. Kim et al. [7] have also found increased NO production in premixed methane-air PAC flames, most likely due to excited metastable species reactions, such as, $O + N_2^* \rightarrow NO + N$. Similar flame stability limit

extension has been reported by Pilla et al [8], who demonstrated significant reduction of the lean flammability limit in a premixed propane-air flame, down to ϕ=0.3.

Repetitively pulsed nanosecond discharge plasmas also serve as an ideal method for study of low rotational-translational temperature, nonequilibrium air chemistry and fuel oxidation kinetics. Similar to traditional flash photolysis sources, nanosecond pulsed discharges in air/fuel mixtures generate initial pools of important radical and metastable state excited species, such as $N_2(A^3\Sigma)$, $O_2(a^1\Delta)$, O, H, and $R\bullet$ (where R represents any hydrocarbon), on time scales of ~0.1-1.0 microseconds. Since the energy directly deposited into translational-rotational modes in such discharges is fairly low, single-pulse or repetitive nanosecond pulsing provides a test bed for the study of low-temperature plasma chemical kinetic processes in air and hydrocarbon-air mixtures. For example, Uddi et al. [9] have used two photon absorption laser induced fluorescence (TALIF) to obtain time and space-resolved measurements of absolute atomic oxygen concentration after initiation of a single-pulse, ~20 kV peak voltage, ~25 nanosecond pulse duration discharge in air, methane-air, and ethene-air mixtures at 60 Torr (7895 Pa). The results were found to agree well with predictions of a hydrocarbon-air plasma chemistry model, supplemented by GRI Mech 3.0 [10**]** and the hydrocarbon oxidation mechanism developed by Wang et al. [11]. In particular, Uddi et al. concluded that O atoms were primarily created by dissociating collisions of ground electronic state O_2 with metastable excited electronic states of N_2, a result which is consistent with that recently reported by Stancu et al. [12,13] who studied an atmospheric pressure, nanosecond pulse discharge in a pin-to-pin electrode configuration. Finally, in a separate study, Uddi et al used single photon Laser Induced Fluorescence (LIF) to determine NO concentration as a function of time after a single 25 nanosecond discharge pulse [14]. It was found that the rise in NO concentration occurred on time scales that were approximately two orders of magnitude too fast to be explained by the well known equilibrium Zeldovich reaction mechanism, but two orders of magnitude too slow to be described by well-known nonequilibirium air chemistry processes, such as reaction of O_2 with electronically excited nitrogen atoms, $N(^2P, ^2D)$. The authors concluded that processes involving reactions of atomic oxygen

with vibrationally excited ground electronic state N_2, such as that discussed by Gordiets et al. [15], and Guerra and Loureiro [16], provide a possible explanation of these recent experimental results.

Single-pulse O atom and $N_2(A^3\Sigma)$ concentration measurements summarized above have served to validate modeling predictions for some of the most important low temperature plasma oxidation processes. However, since the energy coupled to the plasma by a single nanosecond pulse is fairly low (of the order of ~1 mJ/pulse, or ~0.1 mJ/cm^3/pulse), detectable heat release requires from a few tens to a few hundred pulses generated at a high pulse repetition rate (~10-100 pulses/msec). Kinetic mechanism for net energy release in low-temperature hydrocarbon-air plasmas, in excess of that produced directly by the discharge, has not been previously studied in any detail.

In this paper we present time-resolved measurements of rotational-translational temperature rise in air and ethene-air mixtures at 40 torr (5260 Pa) pressure, excited by a burst of 10 to approximately 600 high voltage, nanosecond duration pulses, at 40 kHz pulsed repetition rate. Temperature rise as a function of number of pulses within the burst is determined by pure rotational Coherent Anti-Stokes Raman Scattering (CARS). Experimental results, both in air and in stoichiometric and lean air-fuel mixtures, are found to agree well with plasma chemistry kinetic modeling calculations. The kinetic model incorporates a new model for energy coupling in nanosecond pulse plasmas [17], low-temperature hydrocarbon-air plasma chemistry model, and quasi-one-dimensional heat transfer. In particular, it is found that fairly rapid reactions of ethene with atomic oxygen at room temperature, such as $C_2H_4+O\rightarrow CH_3+HCO$ ($k=4.9\cdot10^{-13}$ cm^3/sec) and $C_2H_4+O\rightarrow CH_2CHO+H$ ($k=2.6\cdot10^{-13}$ cm^3/sec) [10] initiate additional net exothermic plasma chemical fuel oxidation processes, resulting in additional heat release and, under some conditions, ignition.

2. Experimental

The experiments presented here have been conducted in a rectangular cross section quartz channel / plasma flow reactor 220 mm long x 22 mm width x 10 mm height, with 1.75 mm thick walls (see Fig. 1). The measurements have been conducted in dry air and in mixtures of dry air with ethene. Flow rates of air

and fuel are controlled by mass flow controllers at a pressure of 40 torr and a flow velocity of approximately u=0.8 m/sec. Two rectangular copper plate electrodes are attached to the outside of the quartz channel, as shown in Fig. 1. The electrode plates are 14 mm wide by 65 mm long, and are rounded at the corners to reduce the electric field nonuniformity. Room temperature flow residence time in the discharge region is approximately 75 msec, based on the flow velocity of 0.8 m/sec. High voltage, nanosecond pulse discharge (20 kV peak voltage, ~25 nanosecond pulse duration) is generated in air and premixed ethene-air flows using a Chemical Physics Technologies high voltage pulsed power supply. The power supply generates negative polarity pulses, while the terminal connected to the positive electrode can be grounded or left floating. Figure 2 shows typical single-pulse voltage waveforms during a burst of nanosecond pulses in air at 40 Torr and pulse repetition rate 40 kHz (both for pulse #100 in a burst), for grounded and floating discharge operation. It can be seen that leaving the positive terminal floating somewhat reduces the pulse duration (from ~35 nanosecond to ~25 nanosecond for the negative voltage pulse) and considerably reduces voltage oscillations after the pulse, only weakly affecting the peak voltage (22-23 kV). It was also found that leaving the positive terminal floating considerably improved the discharge stability.

For all measurements presented in this paper, the discharge was operated at a 40 kHz pulse repetition rate. In most of the measurements, the pulse generator was operated in a repetitive burst mode, generating sequences of up to 1000 pulses at pulse repetition rate of 40 kHz and burst repetition rate of 10 Hz. This rate matches the pulse repetition rate of the diagnostic lasers, and ensures that each gas sample in the flowing discharge cell experiences only a single burst. To produce breakdown in the discharge section on the first pulse, the test cell was irradiated by a deuterium UV lamp (Resonance Ltd.) through the side wall, providing pre-ionization of the discharge volume. The equivalence ratio in air-fuel mixtures was varied from ϕ=0.1 to 1.0.

A schematic of the pure rotational CARS apparatus, patterned after that of Alden et al. [18], is shown in Fig. 3. Briefly, an Nd:YAG pumped broad-band Ti:sapphire laser, patterned after than of Finkelstein, et al [19] but modified for broad spectral output, with center wavelength of approximately 780 nm and

pulse duration of approximately 15 nanosecond is split into two “pump” beams, with approximately 20 mJ each, and orthogonal linear polarizations. The spectral intensity characteristics of the ti:sapphire output are illustrated in Fig. 4 a-c. Figure 4a shows the spectrum from a typical single ti:sapphire pulse, whereas Figs. 4b and c show 10 and 100 pulse averages, respectively. Note that the longitudinal mode spacing of the ti:sapphire cavity is ~150 MHz (0.005 cm^{-1}) corresponding to ~400,000 modes contained within the Full Width Half Maximum (FWHM) of the spectral profile. While the spectral intensity profile can be seen to be relatively smooth, it is known that phase fluctuations, which cannot be discerned in Fig. 4, contribute significantly to the statistical noise in dual broad band pure rotational CARS spectra [20].

The second harmonic output (532 nm) of a second Nd:YAG laser, with 10 nanosecond pulse duration, is used to generate a horizontally polarized “probe” beam. The pump and probe beams are overlapped in a focused linear phase matching geometry, using a 400 mm focal distance lens. The overlapped focused beams, which propagate parallel to the major axis of the electrodes, form an approximately cylindrically shaped measurement region ~0.1 mm in diameter and 1-2 mm long in the plasma. The pure rotational CARS signal beam is generated with vertical polarization, which allows for very significant (more than a factor of 1000) discrimination from stray, horizontally polarized, probe light using a right angle polarizer. There is, however, a reduction of CARS resonant and non-resonant intensities by a factor of 9/16 and 1/9, respectively. This is most easily seen from eqns. 2, 5, 6, and 7 of Vestin, et al [21]. Skipping the details, the use of this polarization scheme results in zero contribution to the CARS field (both resonant and non-resonant) from susceptibility elements χ_{1122} and χ_{1221}. The magnitude of the remaining χ_{1212} contribution is a factor of ¾ (resonant) and 1/3 (non-resonant) of that when all fields are aligned parallel to one another. This reduced CARS field (both resonant and non-resonant contributions) is aligned parallel to the detection polarizer (ie, orthogonal to probe field), as can be seen from inspection of eq. 7 of reference [21] with $\theta = 90^o$ and $\phi = 0^o$. The CARS beam, after transmission through a short wavelength pass colored glass filter to eliminate residual pump scattering, is focused onto the entrance slit of a ½ meter spectrometer, with an 1800 lines/mm grating and a gated

ICCD camera (Princeton Instruments – PI-MAX). The spectrometer wavelength axis is calibrated using a standard Hg vapor pen lamp. The spectral resolution of the CARS signal is ~1-2 Angstroms. Typically, the CARS signal was averaged over 300 bursts (30 seconds).

Inference of rotational temperature is performed using the Sandia National Laboratories CARS code [20]. Prior to fitting, experimental spectra are corrected to account for the finite spectral width of the Ti:sapphire pump laser. Figure 4d shows the product $I(\nu)\cdot I(\nu+\Delta\nu)$, averaged over the broadband laser spectrum shown in Fig. 4c and normalized to $I^2(\Delta\nu=0) =1$, as a function of $\Delta\nu$. Experimental CARS spectra are divided by this correction factor prior to temperature inference. Note that the Sandia CARS code actually fits the square root of the experimental spectrum, corresponding to the third order susceptibility, also known as χ_{CARS}. Note also that the CARS spectra were modeled as pure air as it was experimentally determined that the contribution of ethene to the pure rotational CARS signal was negligible, even at $\phi = 1$.

In addition to CARS measurements, spatially averaged rotational temperature in the plasma is inferred from visible emission spectra (partially rotationally resolved 0→0 band of the $N_2(C^3\Pi_u \rightarrow B^3\Pi_g)$ band system) as a function of time during the pulse burst. The emission spectroscopy measurement utilizes a ½ meter spectrometer, with a 2400 lines/mm grating, and a gated ICCD camera. Emission spectra were obtained in the range 0 to 20 msec with respect to initiation of a single discharge burst, and averaged over 0.5-1.0 msec (20-40 pulses). The uncertainty of these temperature measurements ranges from $\pm 30^0$ C in air to $\pm 50^0$ C in ethene-air (at T=0-500^0 C) and to ±100-150^0 C in ethene-air (at T~1000^0 C). The uncertainty in CARS inferred rotational temperatures will be discussed in Section 4 below.

Finally, in order to gauge the uniformity of the nanosecond pulsed discharge, the gated ICCD camera was also used to obtain qualitative UV visualization images of a single discharge pulse as a function of pulse number within a burst.

3. Hydrocarbon - Air Nanosecond Pulsed Discharge and Plasma Chemistry Model

The hydrocarbon-air nanosecond pulsed discharge model used in this work is similar to that described by Uddi, et al [9,14]. The air plasma chemistry model incorporates a set of equations for number densities of neutral species (N, N_2, O, O_2, O_3, NO, NO_2, N_2O, NO_3), charged species (e^-, N^+, N_2^+, N_3^+, N_4^+, O^+, O_2^+, O_4^+, NO^+, NO_2^+, N_2O^+, $N_2O_2^+$, N_2NO^+, O_2NO^+, $NONO^+$, O^-, O_2^-, O_3^-, NO^-, NO_2^-, NO_3^-, N_2O^-), and excited species ($N_2(A^3\Sigma)$, $N_2(B^3\Pi)$, $N_2(C^3\Pi)$, $N_2(a'^1\Sigma)$, $O_2(a^1\Delta)$, $O_2(b^1\Sigma)$, $O_2(c^1\Sigma)$, $N(^2D)$, $N(^2P)$, $O(^1D)$) produced in the plasma [23]. The dominant neutral species in air plasmas are the excited electronic states of nitrogen, which are formed by electron impact excitation, and O atoms, which are formed by electron impact dissociation of oxygen and by collisional quenching of excited nitrogen by oxygen, as well as ozone. The species concentration equations are coupled with the two-term expansion Boltzmann equation [24] for the energy distribution function of plasma electrons. The Boltzmann equation solver uses electron impact cross sections [25, 26] and calculates the electron energy distribution function, as well as the rate coefficients of electron impact ionization, dissociation, and electronic excitation, used by the rest of the model. Rate coefficients of remaining kinetic processes in the air plasma, such as electron recombination, attachment and detachment, ion-molecule reactions, and reactions of excited electronic species are taken from [23]. The list of air plasma processes incorporated into the model and their rates is summarized in [14].

To model hydrocarbon-air plasma processes, the air plasma kinetic model was supplemented with methane and ethene dissociation by electron impact and in reactions with electronically excited nitrogen molecules. Cross sections and rate coefficients of these reactions, listed in table 1, were taken from [27-35]. Finally, the plasma model was combined with the hydrocarbon oxidation mechanism, GRI Mech 3.0 [10].

	Process	Rate	Reference
1	$CH_4 + e^- \rightarrow CH_3 + H + e^-$	σ	[27]
2	$N_2(A^3\Sigma) + CH_4 \rightarrow N_2 + CH_3 + H$	$3.3\cdot10^{-15}$ cm^3/s	[29]
3	$N_2(B^3\Pi) + CH_4 \rightarrow N_2 + CH_3 + H$	$3.0\cdot10^{-10}$ cm^3/s	[30]
4	$N_2(C^3\Pi) + CH_4 \rightarrow N_2 + CH_3 + H$	$5.0\cdot10^{-10}$ cm^3/s	[31]
5	$N_2(a'^1\Sigma) + CH_4 \rightarrow N_2 + CH_3 + H$	$3.0\cdot10^{-10}$ cm^3/s	[32]
6	$C_2H_4 + e- \rightarrow products^* + e-$	σ	[28]
7	$N_2(A^3\Sigma) + C_2H_4 \rightarrow N_2 + C_2H_3 + H$	$9.7\cdot10^{-11}$ cm^3/s	[33]
8	$N_2(B^3\Pi) + C_2H_4 \rightarrow N_2 + C_2H_3 + H$	$3.0\cdot10^{-10}$ cm^3/s	estimate
9	$N_2(C^3\Pi) + C_2H_4 \rightarrow N_2 + C_2H_3 + H$	$3.0\cdot10^{-10}$ cm^3/s	estimate
10	$N_2(a'^1\Sigma) + C_2H_4 \rightarrow N_2 + C_2H_3 + H$	$4.0\cdot10^{-10}$ cm^3/s	[35]

Table 1. Fuel species dissociation processes

The high voltage pulse shape used by the plasma chemistry model is a Gaussian fit to the negative polarity voltage pulse shown in Fig. 2. However, due to strong shielding of the applied voltage charge accumulation on the quartz channel walls, the field in the plasma after breakdown is much lower than the applied field. In our previously reported work [9,14], this effect was incorporated by allowing the peak reduced electric field in the pulsed plasma to be an adjustable parameter, chosen to reproduce the experimentally determined peak O atom number density measured in air at P=60 Torr, and T=300K. From the previous work, the best fit value for peak effective reduced electric field was found to be $(E/N)_{peak}$=250 Td (1 Td = 10^{-17} $V\cdot cm^2$), with the corresponding coupled pulse energy of 0.76 mJ. Figure 5, taken from [9] compares time-dependent TALIF O atom concentration measurements in single-pulse nanosecond discharges in air and ethene-air at ϕ=0.5. It can be seen that in both cases, the experimental data is in excellent agreement with the model prediction. It is stressed that no additional adjustable parameters were used to obtain the level of agreement shown for the ethene-air data set, other than the 0.76 mJ coupled pulse energy as determined from the air discharge data. In addition, while not shown, similarly excellent agreement was found for O atom concentration vs time in a stoichiometric methane-air mixture, again excited by a single nanosecond discharge pulse [9].

While the previous results have provided a validation for the critical elements of the air chemistry portions of the model, the hydrocarbon oxidation portion is clearly only partially validated, as O atom

production and loss is just one, albeit important, process in the chain of processes that lead to fuel oxidation and heat release. Since temperature rise in a single discharge pulse under our conditions is estimated to be small, on the order of ~1-2 K, the temperature measurements presented in this paper are performed with the discharge operating in "burst" mode at a high pulse repetition rate.

Kinetic modeling of the burst mode discharge plasma required two key changes in the model. First, as demonstrated in greater detail in a recent paper by Adamovich, et al [17], specific energy coupled to the plasma by a nanosecond discharge pulse (in eV/molecule) remains approximately constant, i.e. coupled pulse energy varies approximately linearly with the number density. Briefly, the nanosecond pulse discharge energy coupling model developed in Ref. [17] incorporates key effects of pulsed breakdown, charge accumulation on dielectric surfaces, and sheath development on nanosecond time scale. Basically, the model predicts that energy coupled to the plasma during an individual nanosecond discharge pulse is controlled primarily by the capacitance of the dielectric layers and by the breakdown voltage. The coupled pulse energy predicted by the nanosecond pulse discharge model in room temperature air is in good agreement with the value inferred from TALIF measurements, 0.76 mJ/pulse [9]. Gradual plasma temperature rise during a pulse burst results in breakdown voltage reduction, thereby decreasing the pulse energy coupled to the plasma as a function of the pulse number in the burst. For the discharge geometry and pulse voltage waveform used in the present work, the coupled pulse energy scales as follows,

$$Q_{coupled} = 0.76 \cdot \left[\frac{p(torr)}{60} \right] \cdot \left[\frac{300}{T(K)} \right] \quad (mJ / pulse) \qquad (1)$$

which is incorporated in the plasma chemistry model by adjusting the peak reduced electric field, $(E/N)_{peak}$. Note that while full coupling of the nanosecond pulse discharge energy coupling model to the plasma chemistry model is in principle possible, it is completely unnecessary, due to the many orders of magnitude difference in characteristic time scales, and would require massive computational resources.

The second model modification accounts for energy loss due to conduction to the quartz channel walls. This is described by incorporating a conduction heat transfer term into the energy equation [17],

$$\frac{dT}{dt} = \dot{q} - \frac{\lambda(T)}{\rho c_p}\frac{(T - T_w)}{(L/\pi)^2} = q\nu_{rep} - \frac{1}{\rho c_p}\sum_i h_i\left(\frac{dn_i}{dt}\right) - \frac{\lambda(T)}{\rho c_p}\frac{(T - T_w)}{(L/\pi)^2} \qquad (2)$$

where $q=Q_{coupled}AL/\rho c_p$ is the coupled pulse energy per unit mass, ν_{rep} is the pulse repetition rate in a burst, h_i are enthalpies of chemical and excited species, dn_i/dt are the rates of species concentrations (in kmole/m^3) change in chemical reactions, $\lambda(T)$ is the thermal conductivity, T_w=300 K is the wall temperature, L is the channel height, and L/π is the spatial scale for conduction heat transfer with uniform generation in the rectangular geometry. Applicability of a 0-D approximation for time-dependent conduction heat transfer was validated by solving separately a 1-D unsteady heat transfer equation [17],

$$\frac{\partial T}{\partial t} = \dot{q} + \frac{1}{\rho c_p}\frac{\partial}{\partial x}\left(\lambda(T)\frac{\partial T}{\partial x}\right) \qquad (3)$$

with the same initial and boundary conditions, and the rate of temperature rise $\dot{q} = q\nu_{rep} - \frac{1}{\rho c_p}\sum_i h_i\left(\frac{dn_i}{dt}\right)$ being the same as predicted by the plasma chemistry model. Comparing the time-dependent plasma temperature, T(t), obtained by the plasma chemistry model using Eq. (2) with the spatially averaged temperature obtained by solving Eq. (3), $\overline{T}(t) = \frac{1}{L}\int_o^L T(x,t)dt$, shows that the difference between them does not exceed a few percent.

4. Results and Discussion

Discharge Uniformity Measurements

Figure 6 shows a collage of broadband ICCD camera images (primarily N_2 second positive band UV/visible emission) of single discharge pulses in pure air at 40 Torr, obtained for different pulse numbers in a burst, ranging from 5 to 600, at a pulse repetition rate of 40 kHz and burst repetition rate of 10 Hz. In these images, the camera gate was 20 microseconds. Note that individual images were taken during different bursts and do not illustrate discharge development during a single burst. While some structure is observed for the first few pulses (e.g. see image of pulse #5), all images for pulse numbers exceeding ~3-5 are observed to be extremely uniform, including images obtained for pulse numbers up to 1000 (25 msec burst duration), which are not shown in Fig. 6. Similar results were obtained for a shorter camera gate, 1 microsecond. Figure 7 is similar to Fig. 6, except the images are obtained in a fuel lean (ϕ = 0.1) ethene-air mixture. In this case the development of a few large scale structures (filaments) in the discharge at pulse numbers ~50-100 is quite apparent. While not shown, comparison of several sets of images obtained from different bursts, but at the same pulse number within the burst, indicates that the filaments develop at random locations within the discharge.

Our previous nanosecond pulse plasma images [17] suggested that filamentation of fuel-air plasmas most likely occurs due to ionization instability development. These results demonstrated that adding either small amounts of ethene (0.07-0.7%, equivalence ratio ϕ=0.01-0.1) or comparable amounts of NO (0.7%) to uniform and stable air plasma readily produced filamentation. Note that both ethene and NO have fairly low ionization potentials, 10.5 eV and 9.3 eV, respectively (compared to nitrogen, 15.6 eV, and oxygen, 12.2 eV). In addition, kinetic modeling of a single pulse nanosecond discharge shows that adding either ethene or NO to air results in more rapid heating by the discharge. It is well known that both lowering the ionization potential and increasing the heating rate contribute to accelerating the rate of ionization / heating instability development [36]. Therefore, both of these factors are likely to play key roles in constriction and filamentation of ethene-air plasmas at these conditions. As can also be seen in Fig. 7, the filaments tend to dissipate after ~400 pulses (10 msec), most likely due to higher thermal

diffusivity, $\lambda/\rho c_p$, at higher temperatures. Diluting the fuel-air mixture with helium, which has much higher thermal diffusivity, resulted in accelerated dissipation of filaments, again suggesting that they are formed due to ionization / heating instability. For ϕ = 1.0 the results are similar, as illustrated in Fig. 8. Again, large scale structures begin to appear after ~50 – 100 pulses and dissipate after ~400 pulses.

Emission Spectroscopy Results

Figure 9 shows experimentally measured time-resolved spatially averaged rotational temperature, inferred from N_2 second positive system emission spectra, in pulsed air plasmas at 40, 60, and 100 Torr, along with kinetic model predictions. ICCD camera imaging [37] showed that the air plasma remains stable and uniform in the entire range of pressures. As discussed in Section 2, each emission spectrum has been accumulated over a period of 0.5 msec (i.e. 20 discharge pulses). As discussed in Section 3, in the modeling calculations coupled pulse energy, $Q_{coupled}$, is scaled proportional to the number density in the plasma (see Eq. (1)). From Fig. 9, it can be seen that after initial rise over 10-20 msec (400-800 pulses), the plasma temperature appears to reach a quasi steady-state, due to increasing heat transfer losses which balance energy loading by the discharge. It can also be seen that the temperature rise becomes more rapid at higher pressures, consistent with the prediction of the nanosecond pulse energy coupling model (see Fig. 1). The results shown in Fig. 9 demonstrate that the air plasma chemistry model accurately reproduces the time-dependent spatially averaged temperature in air plasmas in a wide range of pressures and temperatures, providing validation of both nanosecond pulse energy coupling model and plasma chemistry model.

Figure 10 compares time-resolved spatially averaged temperature in air and in a stoichiometric (ϕ =1) ethene-air mixture at P=40 Torr with kinetic modeling calculations. During these measurements, emission spectra were accumulated over a period of 1 msec (40 discharge pulses). It can be seen that the model appears to underestimate the ethene-air temperature, especially over the first 5 msec (200 pulses). Although the reason for this disagreement is not fully understood, it may be due to spatial non-uniformity of the ethene-air plasma at these conditions, as shown Fig. 8. While not directly relevant, it should also

be noted that at these experimental conditions, no ignition was detected in the test section for bursts up to 25 msec duration (1000 pulses).

Both the emission spectroscopy and modeling calculation results plotted in Fig. 10 suggest that temperature rise in the ethene-air plasma is significantly more rapid than in air, resulting in a temperature difference of approximately 150-200^0 C after 5-10 msec (200-400 pulses). According to the air-fuel plasma chemistry model, since the discharge energy loading per molecule in air and air-fuel plasmas is the same, this difference is the result of additional energy release in exothermic reactions of fuel species with radicals produced by the plasma, primarily O atoms.

Pure Rotational CARS Thermometry Measurements

The reliance on spatially averaged rotational temperatures inferred from emission spectroscopy for air-fuel plasma chemistry studies can be misleading, especially at conditions where heat transfer clearly affects the temperature and may result in significant temperature gradient across the plasma, as illustrated in Figs. 9 and 10. On the other hand, CARS thermometry is a well known diagnostic technique for high spatial and temporal resolution measurement of temperature distributions in flames and plasmas. Figure 11 shows a typical pair of experimental pure rotational CARS spectra in air and in a stoichiometric ethene-air mixture at P=40 Torr. Both spectra are obtained approximately 40 microseconds after a 400 pulse burst at 40 kHz (10 msec burst duration). In these, as well as all subsequent measurements, the laser beams were focused in the center of the discharge (halfway between the top and bottom electrodes, and halfway between the upstream and downstream boundaries of the plasma). The spectra shown in Fig. 11 are averaged over approximately 300 individual laser shots, or over 30 seconds at laser and plasma burst repetition rates of 10 Hz. For burst sequences with higher number of pulses multiple (up to three) accumulations of 300 laser shot spectra are added together to further improve signal to noise, partially compensating for the quadratic dependence of the CARS signal with fluid density. The spectra in Fig. 11 are also normalized to unity at the highest intensity J value. The increase in temperature due to net exothermic plasma-induced fuel oxidation chemistry is readily apparent by comparing the relative

intensities at high J values (i.e. at large Raman shifts of ~100-250 cm^{-1}). Figure 12 shows the square root of the experimental ethene-air CARS spectrum from Fig. 11 along with the best fit synthetic spectrum generated by the Sandia CARS code. While there are some statistical fluctuations that can be seen from the imperfect agreement between the experimental spectrum and best least squares fit, the overall rotational envelop is well reproduced, resulting in an inferred best fit rotational temperature of 860 K. Note that the Sandia CARS code does not provide any estimate of uncertainty in the fitting parameters. We therefore provide an estimate of temperature uncertainty by varying the temperature from that which minimizes the square of the residual between fit and data (χ^2) to that which increases it by 20%. For air and fuel lean spectra this gives an estimated temperature uncertainty of approximately ±25-30 K. For stoichiometric ethene-air spectra, the experimental spectra were somewhat noisier due to what we believe is EMI noise from the pulsed discharge, which tends to accumulate in the ICCD camera approximately proportionately with the total number of discharge pulses experienced during the entire measurement interval. This resulted in temperature uncertainty estimates of approximately ±80-100 K. We are working to reduce EMI pick-up as much as possible.

Figure 13 shows time-resolved air plasma temperatures inferred from emission spectra and CARS as well as the plasma chemistry model predictions for a pulse burst discharge at P=40 Torr and 40 kHz pulse repetition rate. Both emission (i.e. spatially averaged) and CARS (centerline) rotational temperatures are very close to each other until approximately 7.5 msec (300 pulses). After this time, the emission temperature rise becomes slower and starts to level off, indicating significant heat transfer losses, while the CARS temperature continues to increase up to 17 msec (680 pulses). At t=15 msec (600 pulses), the difference between CARS and emission temperature is about 100^0 C. In the kinetic model, the spatially averaged temperature is given by Eq. (2) and the centerline temperature is given by Eq. (3), and there is good agreement between the model and the experiment in each case. Therefore, using a constant wall temperature boundary condition of T_w=300 K in the plasma chemistry/heat transfer model appears to adequately describe the transverse temperature distribution in the air plasma.

Figure 14 compares the CARS temperature with the centerline temperature predicted by the kinetic model in air, lean (φ=0.1), and stoichiometric (φ=1.0) ethene-air mixtures at P=40 Torr and a burst repetition rate of 40 kHz. Both experimental and predicted temperatures are plotted as functions of discharge burst duration. A few general trends are clearly observed. First, comparison of experimental temperatures in air and ethene-air show that the rate of temperature rise in both fuel-air mixtures is much faster than in air during the first 5 msec (200 pulses), approximately 350^0 C versus 125^0 C. Second, the CARS data show that during this stage the rates of heat release in lean and stoichiometric ethene-air mixtures are very close to each other, although the fuel mole fractions differ by a factor of 10. Third, experimental temperatures in air and in the lean ethene-air mixture reach a quasi steady-state at t~15 msec (600 pulses), while temperature in the stoichiometric ethene-air mixture continues to rise.

Two of these trends are well reproduced by the kinetic model. In particular, the model predicts a significantly more rapid centerline temperature rise in air-fuel mixtures than in air, consistent with the CARS data. Also, predicted rates of centerline temperature rise in air-fuel mixtures at ϕ =0.1 and ϕ =1.0 are very close to each other until t=5 msec. However, the model predicts a significantly lower temperature in the stoichiometric air-fuel mixture at t>5 msec than is measured experimentally. Specifically, the model predicts that by 5 msec (200 pulses) the temperature reaches a quasi steady-state, whereas the CARS data indicates that it continues to rise.

To explain these general trends, it is noted that the rate of heat release in the plasma as a function of number of pulses in the burst depends significantly on mixture composition. Figure 15, which plots atomic oxygen and ethene mole fractions predicted by the model in air, lean (ϕ =0.1), and stoichiometric (ϕ =1.0) ethene-air mixtures (i.e. at the conditions of Fig. 14), provides some insight into these trends. In the absence of fuel, O atoms, which are primarily produced by post-discharge collisional quenching of the metastable electronic state of nitrogen, $N_2(A^3\Sigma)$,

$$N_2(A^3\Sigma) + O_2 \rightarrow N_2 + 2\,O \qquad (4)$$

and by electron impact during the discharge pulse,

$$O_2 + e^- \rightarrow O + O + e^- \quad (5)$$

decay relatively slowly in recombination reactions,

$$O + O_2 + M \rightarrow O_3 + M \quad (6)$$

and

$$O + O_3 \rightarrow 2\,O_2 \quad (7)$$

[9]. Note that at low atomic oxygen mole fraction, O atom decay is primarily due to the three-body recombination process (6), whereas as both O atoms and ozone build up, as a result of repetitive pulsing, the rate of the two-body process (7) begins to dominate.

In air, the relatively low rate of recombination results in a considerable build-up of O atoms, to mole fractions of up to ~1%, which is comparable to the 0.7% initial mole fraction of ethene in the lean air-fuel mixture (ϕ =0.1). However, in ethene-air mixtures, O atoms rapidly react with ethene due to the parallel processes,

$$O + C_2H_4 \rightarrow CH_3 + HCO \quad (8)$$

$$O + C_2H_4 \rightarrow H + CH_2CHO \quad (9)$$

which are relatively fast at low temperatures, with 300 K rate coefficients of $k=4.9\cdot10^{-13}$ cm^3/sec and $k=2.6\cdot10^{-13}$ cm^3/sec, respectively [9]. These low-temperature reactions of atomic oxygen with ethene initiate a number of net exothermic hydrocarbon reactions , resulting in accelerated temperature rise, which the model accurately predicts, as can be seen in Fig. 14.

Because of these rapid reactions with ethene, O atom number densities in ethene-air mixtures are much lower than in air under otherwise identical conditions. This can be seen by comparison of the solid red (air) and black (ethene-air, ϕ=1) curves in Fig. 15. Further, as long as fuel is in excess, the rate of chemical energy release (and therefore the rate of temperature rise) in air-fuel mixtures is dictated by the rate of O atom generation (by reactions of Eqs. (4,5)), which is only slightly affected by the ethene mole fraction in the mixture (0.7-6.5%). For this reason, the predicted initial heating rates in the lean and

stoichiometric ethene-air mixtures are very close to each other, which is again consistent with the experimental CARS temperature measurements shown in Fig. 14.

After nearly all fuel in the lean mixture has been oxidized (after ~200 discharge pulses, or ~5 msec), the heating rate is predicted to slow down, and, simultaneously, the O atom number density is predicted to start rising rapidly. This is illustrated in Fig. 14 (heating rate reduction) and Fig. 15 (O atom build-up), respectively. However, since the stoichiometric mixture has ten times more fuel, its mole fraction remains approximately constant (dashed black curve in Fig. 15), as does the corresponding predicted heating rate. For this reason, the stoichiometric mixture continue to generate additional heat as the number of pulses increases beyond ~200–400 (5–10 msec). The most likely reason for the significant difference between experimental and predicted centerline temperatures in the stoichiometric mixture after large number of pulses (~400 pulses, or ~10 msec) is heating of the test section walls. At these conditions, the use of the constant wall temperature boundary condition (T_w=300 K) is likely no longer justified, since the rate of heat transfer from the plasma to the cold wall is significantly overestimated. Further temperature measurements, using a vertical translation stage to move the discharge cell relative to the fixed CARS beams, will study this effect in greater detail.

Finally, Fig. 16, taken from Uddi, et al. [36] compares previously measured O atom number densities in air, stoichiometric methane-air, and lean (ϕ = 0.5) ethene-air at P=60 Torr as a function of number of pulses in a burst with predictions of the kinetic model used in the present work. These measurements were taken using a different plasma generator (FID Technology) than that used in the present work, and at a different pulse repetition rate (100 kHz). However, it can be seen that the model is in good agreement with all three experimental data sets, predicting accumulation of O atoms in air of up to $4 \cdot 10^{15}$ cm^{-3} (0.2% mole fraction) over 1 msec (100 pulses), and much lower O atom concentration in ϕ = 0.5 ethene-air, after the same number of pulses, by approximately two orders of magnitude. In fact, the data shown in Fig. 16 confirms that the rate of O atom production in ethene-air is essentially equal to the rate of loss, due to the relatively fast rates of processes of Eqs. (8,9). Note also that while not studied in the present work, the rate of loss of O atoms via reaction with methane at room temperature has been confirmed to be many

orders of magnitude lower than with ethene [9]. This is reflected in the observed build-up of O atoms during the burst, to a value intermediate between that of measured in air and in an ethene-air mixture.

5. Summary and Conclusions

Time-resolved rotational temperature in a repetitively pulsed nanosecond discharge operated in burst mode in air and in ethene-air mixtures has been measured by purely rotational CARS. The results are compared to the low-temperature hydrocarbon-air plasma chemistry model predictions. The plasma chemistry model, developed in our previous work, has been validated by a series of atomic oxygen mole fraction measurements taken in low temperature air, and ethene-air nanosecond pulsed plasmas. In the present work, the plasma chemistry model has been modified to incorporate non-empirical scaling of the nanosecond discharge pulse energy coupled to the plasma with the number density, as well as one-dimensional conduction heat transfer. These modifications allow prediction of time-dependent temperature distribution across the plasma, without the use of the pulse energy as an adjustable parameter.

The rate of heat release, and corresponding temperature rise, as a function of the number of pulses in a burst, was predicted by the model and found to agree well with centerline pure rotational time-resolved CARS temperature measurements, in air and in ethene-air mixtures at $\phi = 0.1$ and $\phi = 1.0$. Comparison of centerline CARS temperatures and spatially averaged temperatures inferred from N_2 second positive emission spectra confirm that at long discharge burst duration, temperature distribution in the plasma is strongly affected by heat transfer.

Both CARS measurements and the air-fuel plasma chemistry model predictions show accelerated heating in ethene-air mixtures due to heat release during plasma chemical fuel oxidation, which is triggered by relatively fast low temperature reactions of ethene with atomic oxygen. The initial heating rate in air-fuel plasmas is primarily controlled by the rate of radical, particularly O atom, generation, and is nearly independent of the equivalence ratio. At long burst durations, the heating rate in lean ethene-air mixtures is significantly reduced at the point when nearly all of the fuel is oxidized. On the other hand,

temperature in the stoichiometric ethene-air mixture continues to rise even for long burst durations due to continuous fuel oxidation / energy release process. Experimental centerline temperatures in stoichiometric ethene-air mixtures at long burst durations are observed to be higher than predicted by the model, likely due to the use of a cold wall (T_w=300 K) boundary condition by the model, which over predicts the rate of heat transfer from the plasma thermal to the test section walls.

Future work will include additional CARS temperature measurements at multiple locations (above and below centerline, and closer to the edges of the plasma) and additional O atom concentration measurements during burst mode discharge operation, particularly in lean ethene-air mixtures.

Acknowledgements

The authors wish to acknowledge the sponsorship of the U.S. Air Force Office of Scientific Research (Julian Tishkoff – Technical Monitor) and the National Science Foundation (Phillip Westmoreland – Technical Monitor) for support of this research.

References

[1] Starikovskaia SM 2006 Plasma assisted ignition and combustion 2006 *J. Phys. D. Appl. Phys* **39** R265-R299.

[2] I.V. Adamovich, I. Choi, N. Jiang, J.-H Kim, S. Keshav, W.R. Lempert, E. Mintusov, M. Nishihara, M. Samimy, and M. Uddi, "Plasma Assisted Ignition and High-Speed Flow Control: Non-Thermal and Thermal Effects", *Plasma Sources Science and Technology*, vol. 18, 2009, p. 034018

[3] A. Hicks, S. Tirupathi, N. Jiang, Yu. Utkin, W.R. Lempert, J.W. Rich, and I.V. Adamovich, "Design and Operation of a Supersonic Flow Cavity for a Non-Self-Sustained Electric Discharge Pumped Oxygen-Iodine Laser", *Journal of Physics D: Applied Physics*, vol. 40, 2007, pp. 1408-1415

[4] Starikovski AY 2005 Plasma supported combustion *Proceedings of the Combustion Institute* **30** 2405-2417.

[5] Bozhenkov SA, Starikovskaya SM and Starikovskii AYu 2003 Nanosecond gas discharge ignition of H2 and CH4 containing mixtures *Combustion and Flame* **133** 133-146.

[6] Kim W, Do H, Mungal MG and Cappelli M 2006 Plasma-Discharge Stabilization of Jet Diffusion Flames *IEEE Trans on Plasma Science* **34** 2545-2551.

[7] Kim W, Do H, Mungal MG and Cappelli M, 2007 Investigation of NO production and flame structure in plasma enhanced premixed combustion *Proceedings of Combustion Institute* **31** 3319-3326.

[8] G. Pilla, D. Galley, D.A. Lacoste, F. Lacas, D. Veynante, and C.O. Laux, "Stabilization of a Turbulent Premixed Flame Using a Nanosecond Repetitively Pulsed Plasma", *IEEE Trans. Plasma Sci.*, vol. 34, 2006, p. 2471

[9] Uddi M, Jiang N, Mintusov E, Adamovich IV and Lempert WR 2009 Atomic Oxygen Measurements in Air and Air/Fuel Nanosecond Pulse Discharges by Two Photon Laser Induced Fluorescence *Proceedings of Combustion Institute* **32** 929-936.

[10] http://www.me.berkeley.edu/gri_mech/version30/text30.html, GRI-Mech 3.0

[11] Wang H, You X, Joshi AV, Davis SG, Laskin A, Egolfopouls F, and Law CK 2007 USC Mech Version II. High-Temperature Combustion Reaction Model of H2/CO/C1-C4 Compounds. http://ignis.usc.edu/USC_Mech_II.htm.

[12] Stancu GD, Janda M, Kaddouri F, Pai D, Lacoste DA, Rolon JC and Laux CO 2008 *AIAA-2008-3882* 39th AIAA Plasmadynamics and Lasers Conference 23 - 26 June 2008, Seattle, WA

[13] Stancu GD, Kaddouri F, Lacoste DA and Laux CO 2009 Investigations of rapid plasma chemistry generated by nanosecond discharges in air at atmospheric pressure using advanced optical diagnostics *AIAA-2009-3593* 40th AIAA Plasmadynamics and Lasers Conference, 22-25 June, 2009, San Antonio, TX.

[14] Uddi M, Jiang N, Adamovich IV, Lempert WR, 2009 Nitric Oxide Density Measurements in Air and Air/Fuel Nanosecond Pulse Discharges by Laser Induced Fluorescence *J. Phys. D Appl. Phys.* **42** 075205-075222.

[15] Gordiets BF, Ferreira CM, Guerra VL, Loureiro L, Nahorny J, Pagnon D, Touzeau M, and Vialle M Kinetic Model of a Low Pressure N_2-O_2 Flowing Flow Discharge 1995 *IEEE Trans. Plasma Sci.* **23** 750-768.

[16] Guerra V, Sa PA, and Loureiro J. 2001 Role Played by the $N_2(A^3\Sigma_u^+)$ Metastable in Stationary N_2 and N_2-O_2 Discharges *J. Phys. D: J. Appl. Phys.*, **34** 1745–1755.

[17] Adamovich IV, Nishihara M, Choi I, Uddi M, and Lempert WR 2009 Energy Coupling to the Plasma in Repetitive Nanosecond Pulse Discharges, accepted for publication in Physics of Plasmas.

[18] Alden M, Bengtsson PE and Edner H 1986 Rotational CARS generation through a multiple four-color interaction *Appl. Opt.* **25** 4493-4500.

[19] Finkelstein N, Gambogi J, Lempert WR, Miles RB, Rines GA, Finch A, and Schwarz RA 1994, The Development of a Tunable, Single-Frequency Ultraviolet Laser Source for UV Filtered Rayleigh Scattering, Paper #AIAA-94-0492, AIAA 32nd Aerospace Sciences Meeting & Exhibit, Reno, Nevada.

[20] Alden M, Bengtsson P-E, Edner H, Kroll S, and Nilsson D 1989 Rotational CARS: a comparison of different techniques with emphasis on accuracy in temperature determination *Appl. Opt.* **28** 3206-3219.

[21] Vestin F, Afselius M, and Bengtsson P-E 2007 Development of rotational CARS for combustion diagnostics using a polarization approach *Proceedings of Combustion Institute* **31** 833-840.

[22] Palmer R, Sandia National Laboratories – Combustion Research Facility.

[23] Kossyi IA, Kostinsky AY, Matveyev AA and Silakov VP 1992 Kinetic Scheme of the Nonequilibrium Discharge in Nitrogen-Oxygen Mixtures *Plasma Sources Science and Technology* **1** 207-220.

[24] Huxley LGH and Crompton RW 1974 *"The Diffusion and Drift of Electrons in Gases"*, Wiley, New York.

[25] Itikawa Y, Hayashi M, Ichimura A, Onda K, Sakimoto K, Takayanagi K, Nakamura M, Nishimura M and Takayanagi T 1986 Cross Sections for Collisions of Electrons and Photons with Nitrogen Molecules, *J. Phys. Chem. Ref. Data* **16** 985-1010.

[26] Itikawa Y, Ichimura A, Onda K, Sakimoto K, Takayanagi K, Hatano Y, Hayashi M, Nishimura H, and Tsurubichi S, J. 1989 Cross Sections for Collisions of Electrons and Photons with Oxygen Molecules *Phys. Chem. Ref. Data* **18** 23-42.

[27] Motlagh S and Morre J, 1989 Cross Sections for Radicals from Electron Impact on Methane and Fluoroalkanes *J. Chem. Phys*. **109** 432-438.

[28] Janev RK and Reiter D 2004 Collision Processes of $C_{2,3}H_y$ and $C_{2,3}H_y^+$ hydrocarbons with Electrons and Protons *Physics of Plasmas* **11** 781-829.

[29] Golde MF, Ho GH, Tao W and Thomas JM 1989 Collision Deactivation of $N_2(A^3\Sigma_u^+$, v=0-6) by CH_4, CF_4, H_2, H_2O, CF_3Cl, and CF_2HCl *J. Phys. Chem.* **93** 1112-1118.

[30] Piper LG, *J. Chem. Phys.* 1992 Energy Transfer Studies on $N_2(X^1\Sigma_g^+$,v) and $N_2(B^3\Pi_g)$ **97** 270-275.

[31] Albugues F, Birot A, Blanc D, Brunet H, Galy J, Millet P and Teyssier JL 1974 Destruction of the Levels $C^3\Pi_u$ (v´=0, v´=1) of nitrogen by O_2, CO_2, CH_4, and H_2O *J. Chem. Phys.* **61** 2695-2699.

[32] Umemoto H, Ozeki R, Ueda M and Oku M 2002 Reactions of $N_2(a'^1\Sigma_u^-)$ with H_2, CH_4, and Their Isotopic Variants: Rate Constants and the Production Yield of H(D) atoms *J. Chem. Phys.* **117** 5654-5659.

[33] Thomas JM, Kaufman F, Golde MF 1987 Rate Constants for Electronic Quenching of $N_2(A^3\Sigma_u^+$, v=0-6) by O_2, NO, CO, N_2O, and C_2H_4 *J. Phys. Chem.* **86** 6885-6892.

[34] Fresnet F, Baravian G, Magne L, Pasquiers S, Postel C, Peuch V and Rousseau A 2000 Kinetic of the NO Removal by Nonthermal Plasma in $N_2/NO/C_2H_4$ Mixtures *Appl. Phys. Lett.* **77** 4118-4120.

[35] Umemoto H, J. 2007 Production Yields of H(D) Atoms in the Reactions of $N_2(A^3\Sigma_u^+)$ with C_2H_2, C_2H_4, and Their Deuterated Variants *Chem. Phys.* **127** 014304.

[36] Yu.P. Raizer, "Gas Discharge Physics", Springer-Verlag, Berlin, 1991.

[37] I. Choi, M. Uddi, Y. Zuzeek, I.V. Adamovich, and W.R. Lempert, "Stability and Heating Rate of Air and Ethene-Air Plasmas Sustained by Repetitive Nanosecond Pulses", AIAA Paper 2009-0688, 47th Aerospace Sciences Meeting and Exhibit, 5-8 January 2009, Orlando, FL.

[38] M. Uddi, N. Jiang, E. Mintusov, I. V. Adamovich, and W. R. Lempert, "Atomic Oxygen Measurements in Air and Air/Fuel Nanosecond Pulse Discharges by Two Photon Laser Induced Fluorescence", AIAA Paper 2008-1110, 46th Aerospace Sciences Meeting and Exhibit, 7-10 January 2008, Reno, NV.

Figure Captions

Figure 1: Schematic of optical access discharge test section / flow reactor

Figure 2: Typical single-pulse voltage waveforms during a burst of nanosecond pulses in air at 40 torr and pulse repetition rate 40 kHz (pulse #100 in a burst), for grounded and floating discharge operation.

Figure 3: Schematic diagram of pure rotational CARS apparatus. Electrodes are above/below plane of paper

Figure 4: Broadband Ti:sapphire spectral output (left) and intensity squared correction factor for experimental CARS spectra (right).

Figure 5: O atom mole fraction vs. time after a single high-voltage pulse in air, in methane-air (ϕ=1.0), and in an ethene-air (ϕ=0.5) mixtures at P=60 Torr [9]. Pulse energy used in modeling calculations 0.76 mJ.

Figure 6: Collage of broadband ICCD camera images (primarily N_2 second positive system emission) of individual discharge pulses in air at 40 Torr, obtained during burst mode operation. Discharge pulse repetition rate is 40 kHz, burst repetition rate 10 Hz, camera gate 20 microseconds.

Figure 7: Collage of broadband ICCD camera images of individual discharge pulses in fuel lean (ϕ=0.1) ethene-air mixture at 40 Torr, obtained during burst mode operation. Discharge pulse repetition rate is 40 kHz, burst repetition rate 10 Hz, camera gate 20 microseconds.

Figure 8: Collage of broadband ICCD camera images of individual discharge pulses in stoichiometric (ϕ=1.0) ethene-air mixture at T0 torr, obtained during burst mode operation. Discharge pulse repetition rate is 40 kHz, burst repetition rate 10 Hz, camera gate 20 microseconds.

Figure 9: Comparison of experimental spatially averaged (emission) temperatures in a repetitively pulsed nanosecond discharge in air with the plasma chemistry model prediction at different pressures.

Figure 10: Comparison of experimental spatially averaged (emission) temperatures in a repetitively pulsed nanosecond discharge in air and in ethene-air (ϕ=1.0) at P=40 Torr with the plasma chemistry model prediction.

Figure 11: Typical rotational CARS spectra in air and ethene-air (ϕ=1) after a 400 pulse burst at 40 kHz (burst duration 10 msec). P=40 Torr. Each spectrum is normalized to peak rotational line intensity.

Figure 12: Experimental and synthetic rotational CARS spectra in ethene-air (ϕ=1) at the conditions of Fig. 12. Inferred rotational temperature T=860±50 K.

Figure 13: Comparison of experimental spatially averaged (emission) and centerline (CARS) temperatures in a repetitively pulsed nanosecond discharge in air at P=40 torr with the plasma chemistry model prediction.

Figure 14: Comparison of experimental centerline (CARS) temperatures in a repetitively pulsed nanosecond discharge in air and in ethene-air (ϕ=0.1 and ϕ =1.0) at P=40 Torr with the plasma chemistry model prediction.

Figure 15: Plasma chemistry model predictions for O (solid curves) and ethene (dashed curves) mole fractions for air and ethene-air mixtures.

Figure 16: O atom number density vs. number of pulses in burst in air, in methane-air (ϕ=1.0), and in an ethene-air (ϕ=0.5) mixtures at P=60 Torr and ν=100 kHz.

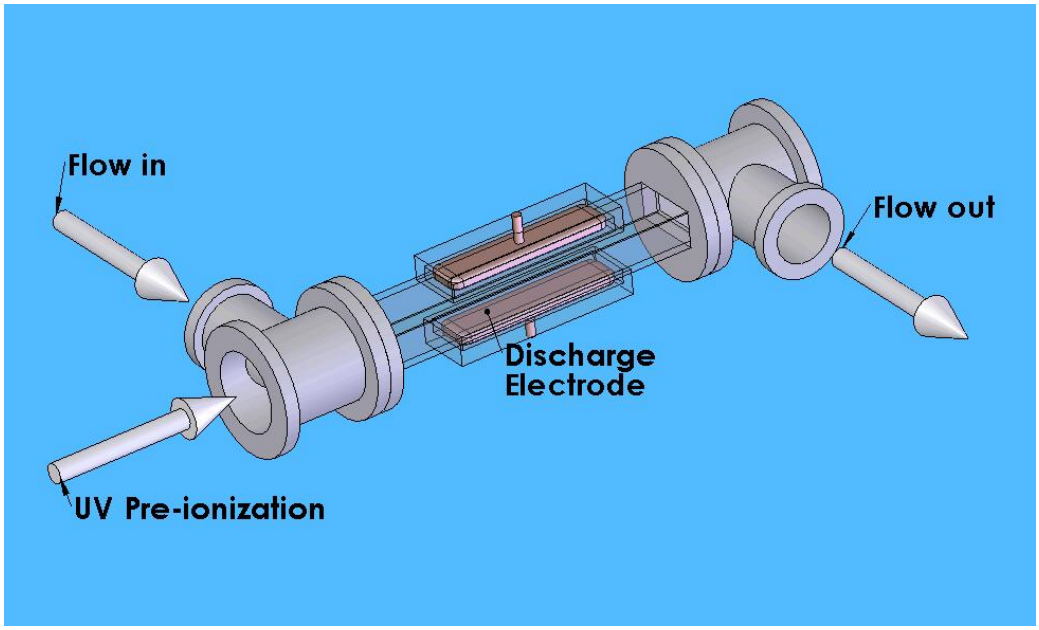

Zuzeek – Figure 1

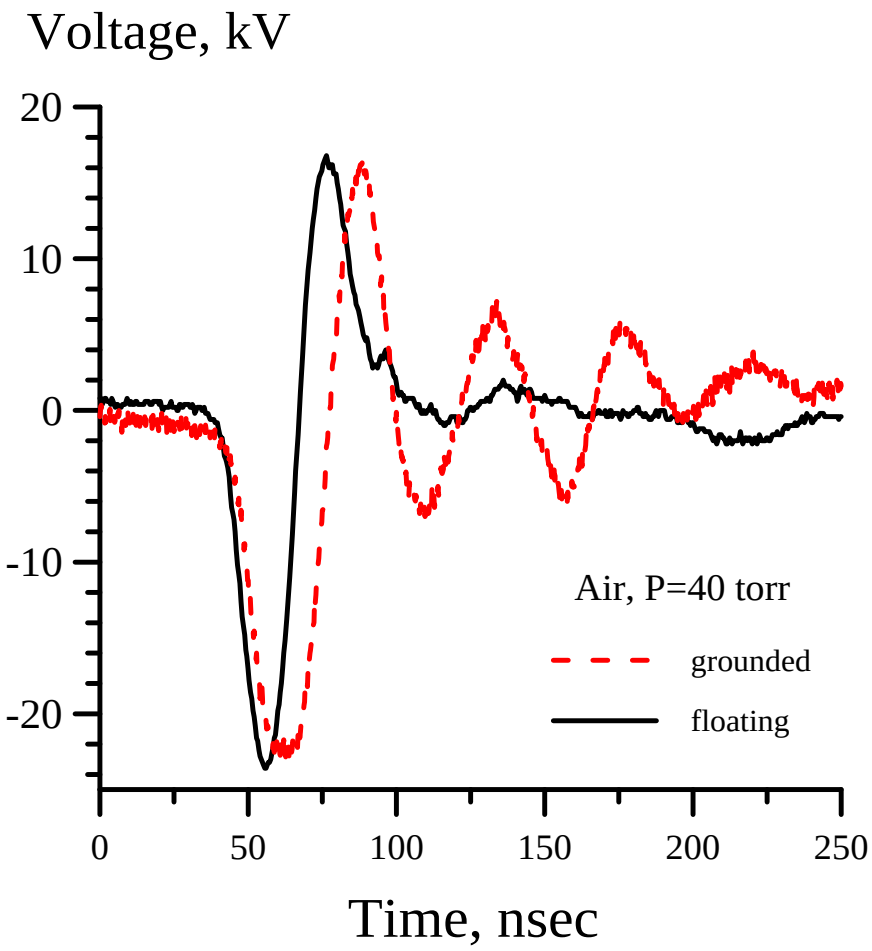

Zuzeek – Figure 2

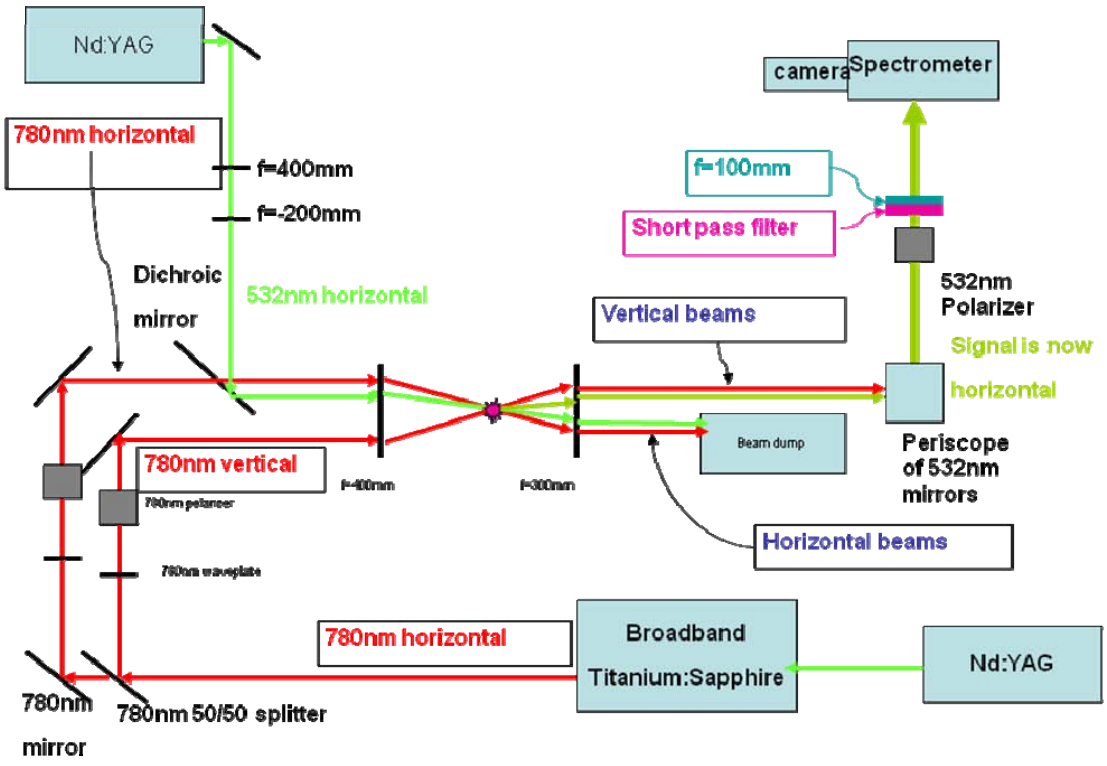

Zuzeek – Figure 3

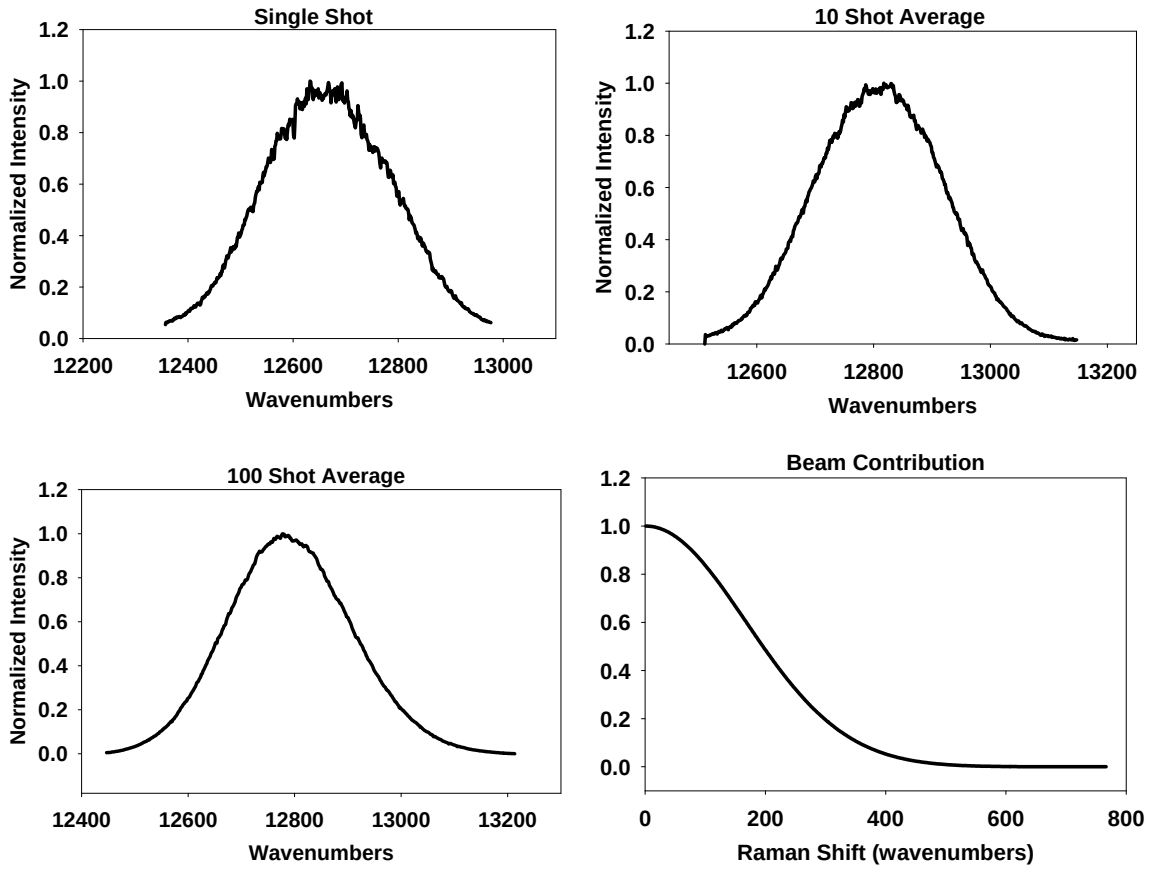

Zuzeek – Figure 4

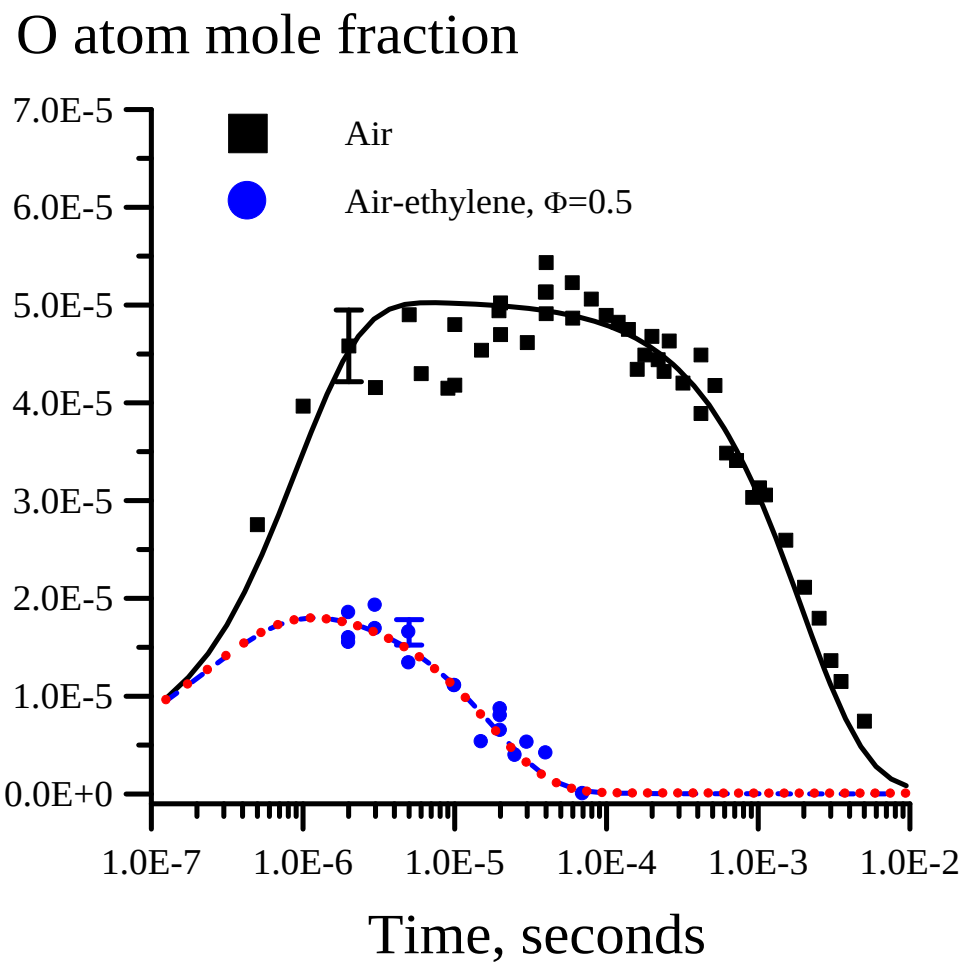

Zuzeek – Figure 5

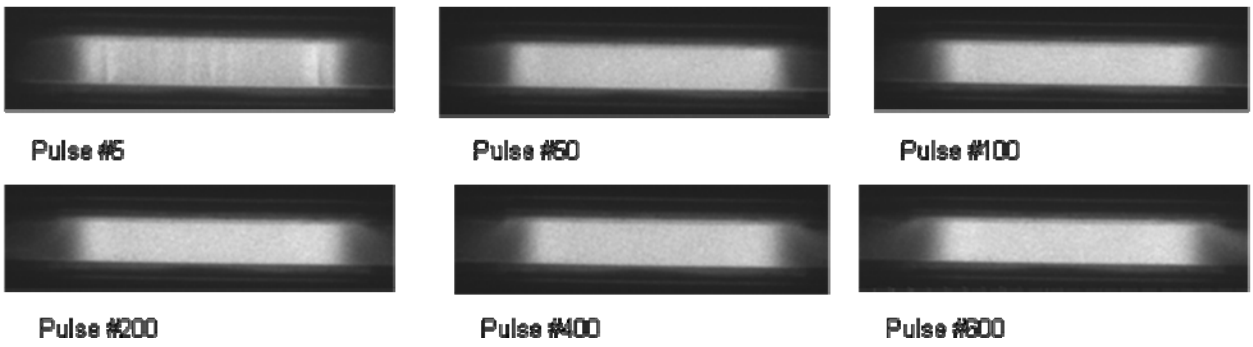

Zuzeek – Figure 6

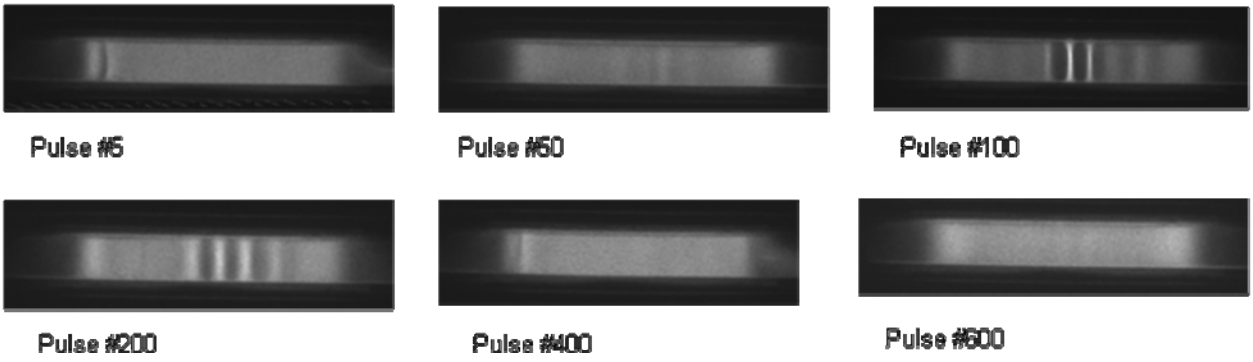

Zuzeek – Figure 7

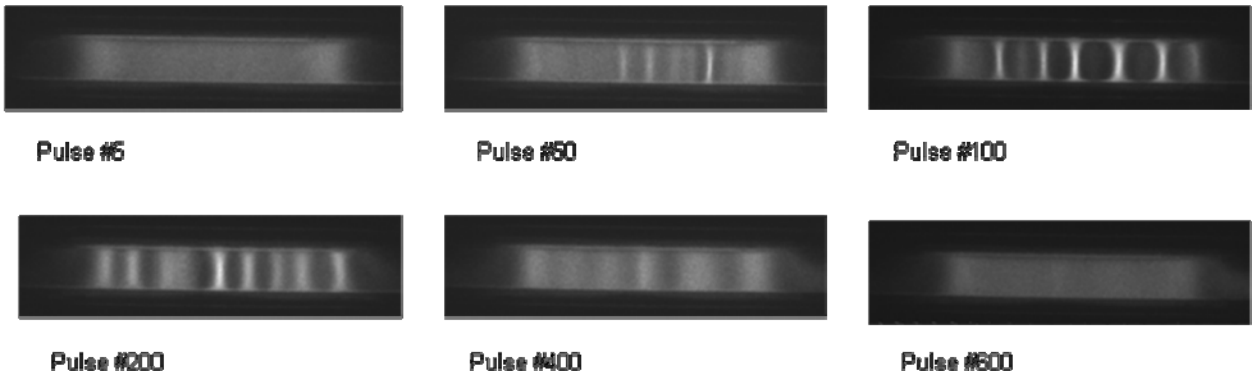

Zuzeek – Figure 8

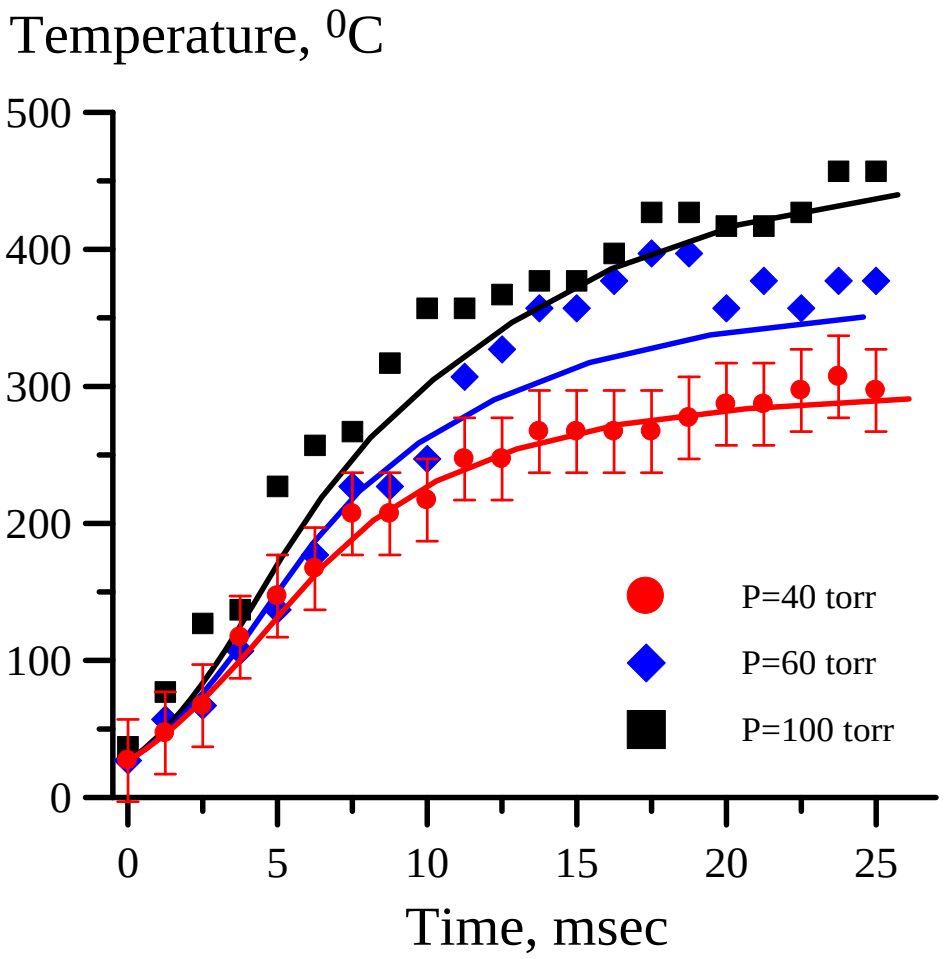

Zuzeek – Figure 9

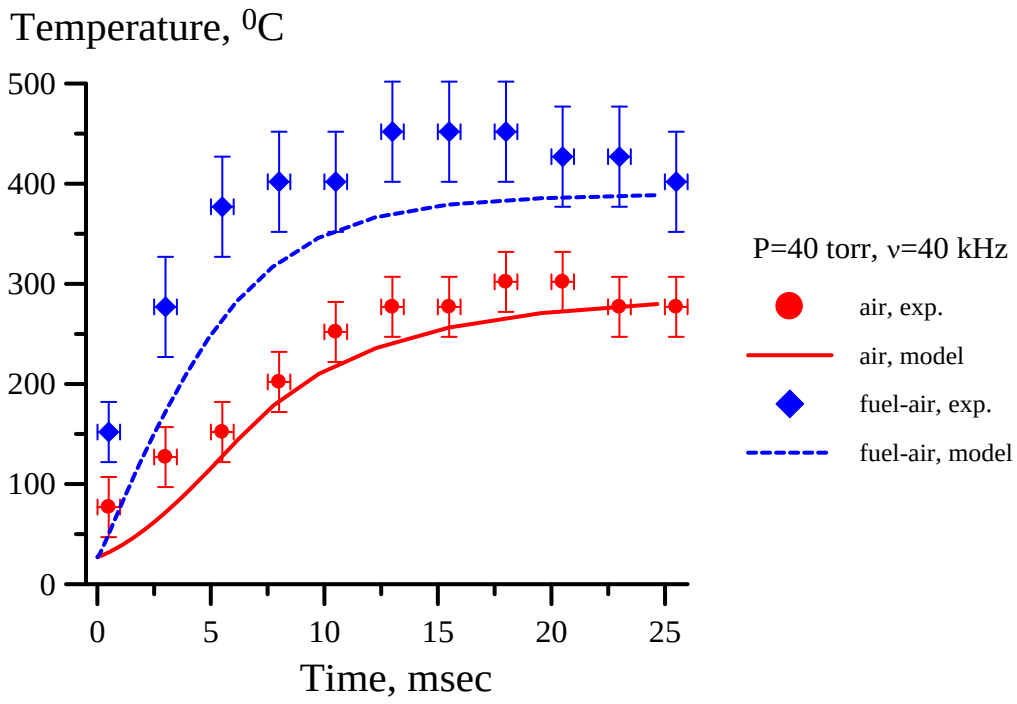

Zuzeek – Figure 10

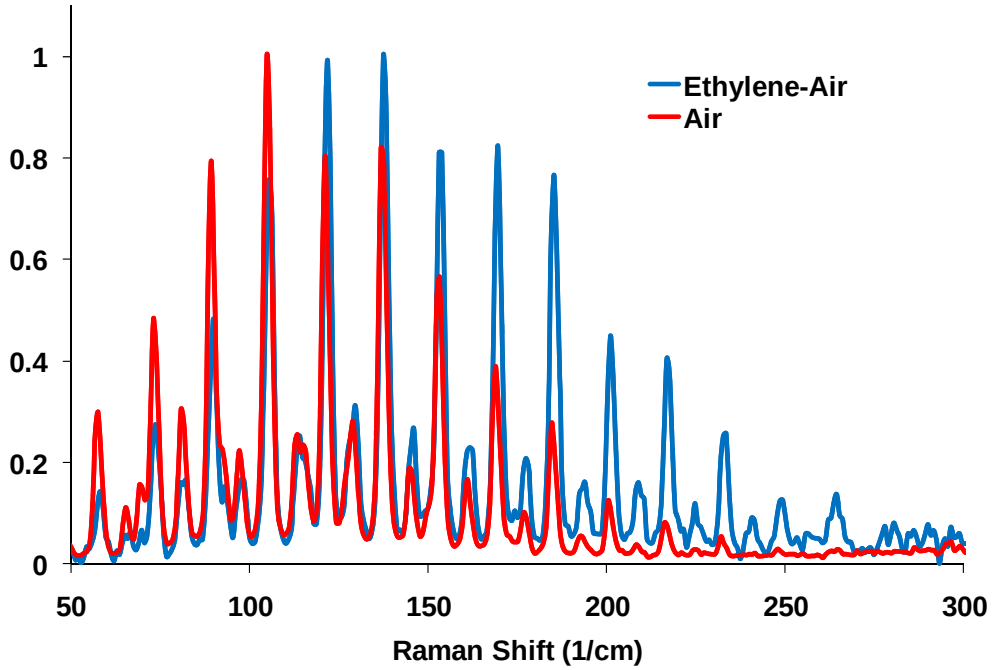

Zuzeek – Figure 11

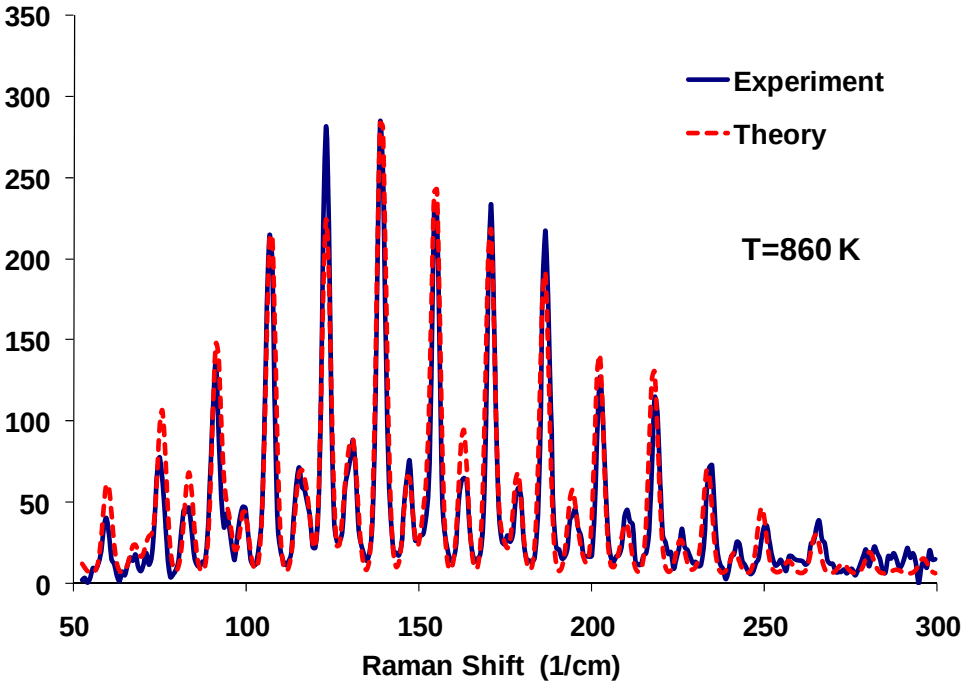

Zuzeek – Figure 12

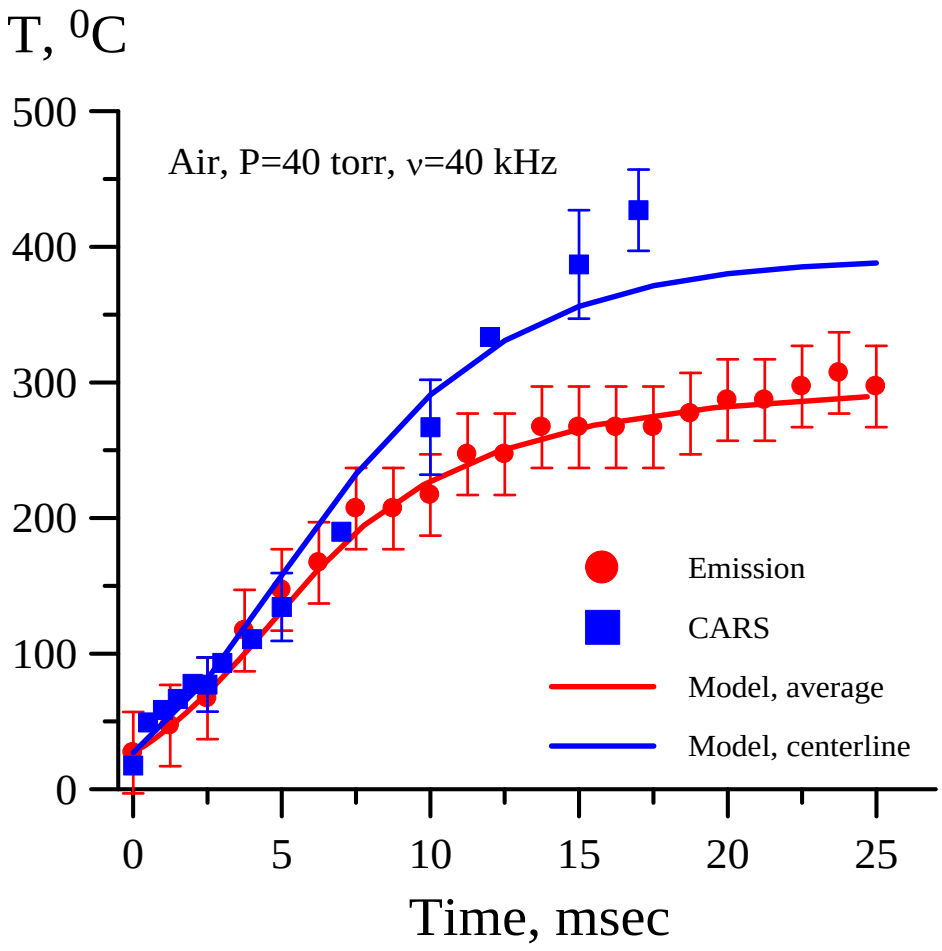

Zuzeek – Figure 13

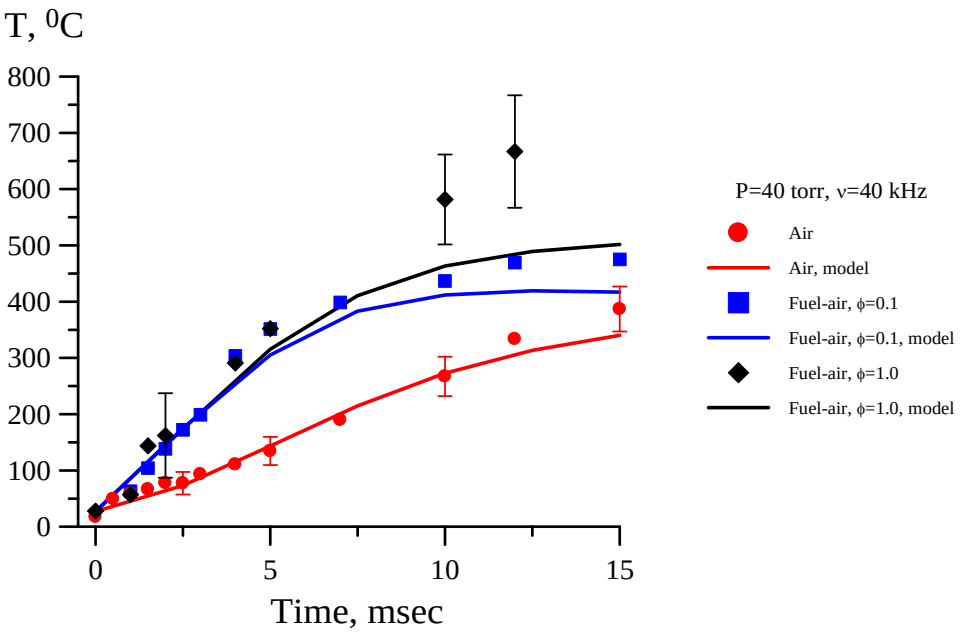

Zuzeek – Figure 14

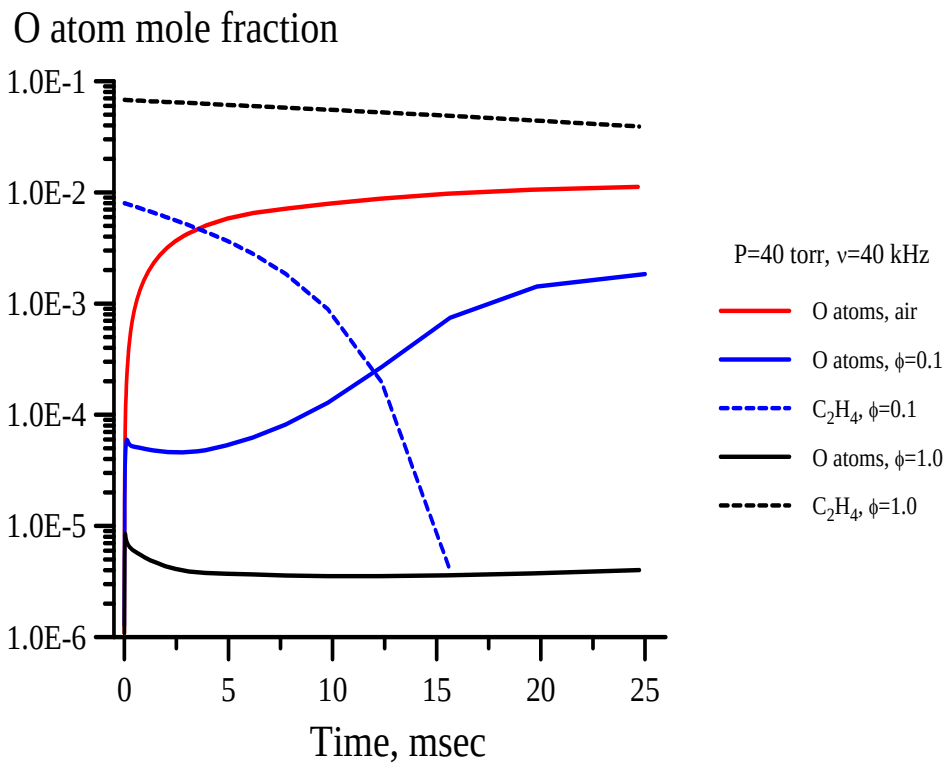

Zuzeek – Figure 15

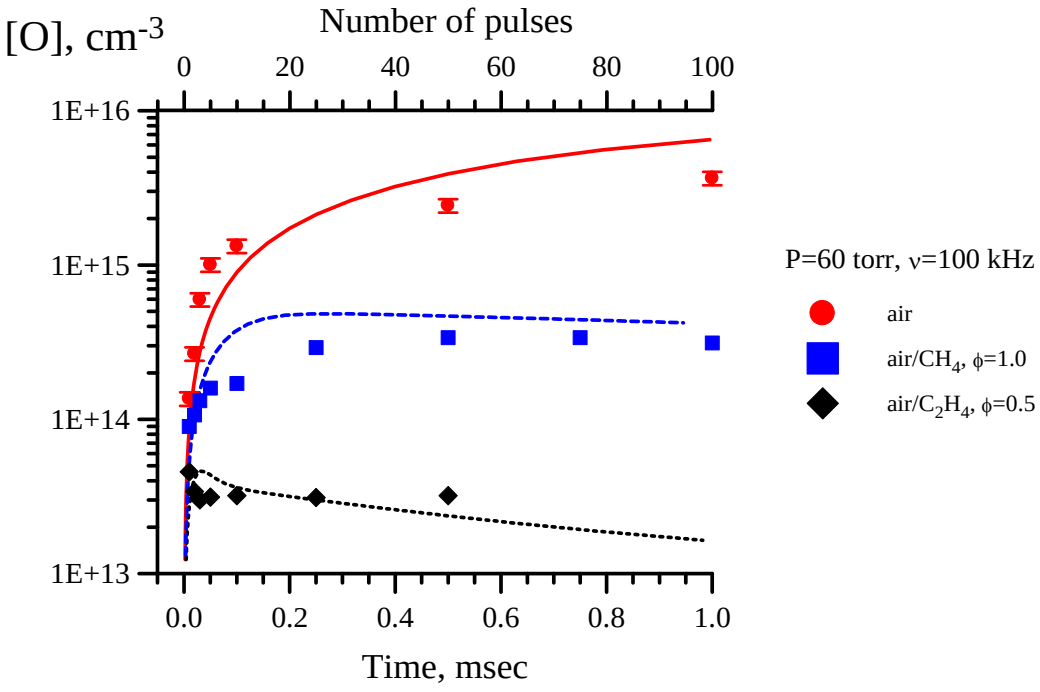

Zuzeek – Figure 16